JGR Oceans

RESEARCH ARTICLE
10.1029/2019JC015383

Key Points:
- Kelvin-Helmholtz billows growing on a lutocline are observed for the first time
- Linear instability theory can successfully predict characteristics of the billows
- The instabilities have the potential to modify estuarine sediment transport processes

Supporting Information:
- Supporting Information S1
- Data Set S1
- Data Set S2

Correspondence to:
D. Fan and W. Smyth,
ddfan@tongji.edu.cn;
bill.smyth@oregonstate.edu

Citation:
Tu, J., Fan, D., Lian, Q., Liu, Z., Liu, W., Kaminski, A., & Smyth, W. (2020). Acoustic observations of Kelvin-Helmholtz billows on an estuarine lutocline. *Journal of Geophysical Research: Oceans*, *125*, e2019JC015383. https://doi.org/10.1029/2019JC015383

Received 13 JUN 2019
Accepted 18 MAR 2020
Accepted article online 24 MAR 2020

Acoustic Observations of Kelvin-Helmholtz Billows on an Estuarine Lutocline

Junbiao Tu[1], Daidu Fan[1,2], Qiang Lian[3], Zhiyu Liu[3], Wei Liu[1], Alexis Kaminski[4], and William Smyth[5]

[1]State Key Laboratory of Marine Geology, Tongji University, Shanghai, China, [2]Laboratory of Marine Geology, Qingdao National Laboratory for Marine Science and Technology, Qingdao, China, [3]State Key Laboratory of Marine Environmental Science, and Department of Physical Oceanography, College of Ocean and Earth Sciences, Xiamen University, Xiamen, China, [4]Applied Physics Laboratory, University of Washington, Seattle, WA, USA, [5]College of Oceanic and Atmospheric Sciences, Oregon State University, Corvallis, OR, USA

Abstract Kelvin-Helmholtz (KH) instability plays an important role in turbulent mixing in deep oceans, coastal seas, and estuaries. Though widely observed and studied in thermohaline-stratified waters, KH instability has only rarely been observed in sediment-stratified environments. For the first time, we present direct observations of KH billows on an estuarine lutocline by combining echosounder images with velocity and density measurements. The interaction between velocity shear and the density stratification induced by suspended sediments initiated shear instabilities near the bed, indicated by gradient Richardson number (Ri) < 0.25 in the early stages of the observed billows. Once formed, the instabilities enhanced the vertical mixing of momentum, reducing vertical shear and elevating Ri. Linear instability analysis using measured velocity and density profiles well predicts the vertical location and spatial characteristics of the observed billows. These instabilities are believed to contribute to the vertical mixing, entrainment, and transport of estuarine and coastal sediments.

1. Introduction

In this study, acoustic observations of shear instability on an estuarine lutocline will be presented and analyzed. Shear instability is an important mechanism for the development of turbulence and mixing in the stratified oceanic interior and coastal seas (Smyth & Moum, 2012). It has been widely identified in thermohaline-stratified environments, including both estuarine and open-ocean sites, most often by means of echosounder images (Geyer et al., 2010, 2017; Geyer & Smith, 1987; Holleman et al., 2016; Lavery et al., 2013; Tedford et al., 2009) but also using sequential temperature profiles (Hebert et al., 1992; van Haren et al., 2014).

In high-energy, turbid estuarine and coastal environments, large density gradients due to suspended sediment usually separate the water into two layers with distinctly different densities. The intervening layer of large gradient has been termed the lutocline (Kirby & Parker, 1983). In analogy to its thermohaline counterpart, this sediment-stratified layer is susceptible to instabilities when the shear across it is sufficiently strong.

Kelvin-Helmholtz (KH) instability, the most common class of shear instability, is generally recognized by its alternating braid-core structure in echosounder images (Geyer et al., 2010). Instabilities may also have a vertically asymmetric form, cusped at the crests or the troughs but not both. When the shear is distributed over a thicker layer than the stratification, as is common when molecular viscosity exceeds diffusivity, the Holmboe variety of shear instability may be observed (Lawrence et al., 1998). The Holmboe mechanism can also create asymmetric structures resembling KH billows (Carpenter et al., 2010).

In benthic boundary layers in hyperturbid environments, observation is challenging and the instabilities, if any, are difficult to identify due to their limited scale and insufficient sensor resolution. In laboratory experiments, KH billows were observed along the interface of the fluid mud and overlying water (Scarlatos & Mehta, 1993). In a mudflat channel, instability was inferred based on measurements of flow velocity and turbidity but was not documented directly (Adams et al., 1990). Held et al. (2019, 2013) documented asymmetrically cusped waves in the Ems Estuary which they identified as Holmboe instability (e.g., Carpenter et

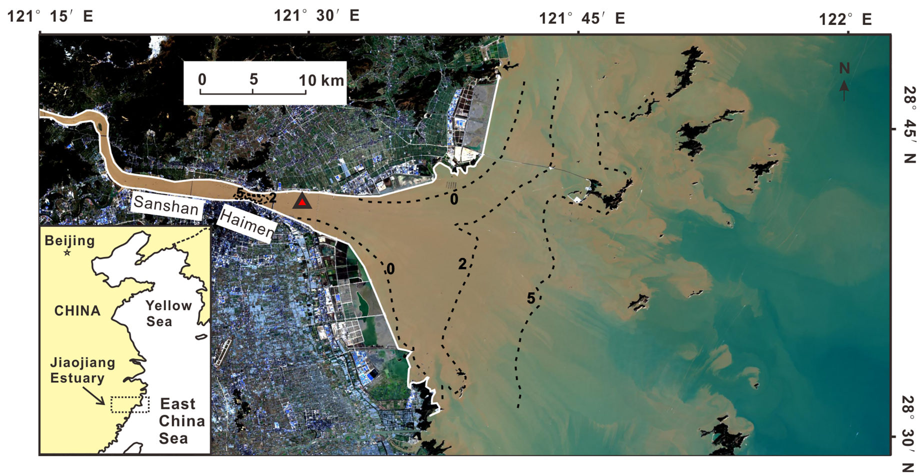

Figure 1. Study area, satellite image courtesy (https://glovis.usgs.gov/app?fullscreen=0). The triangle shows the location of observational site.

al., 2007). In this study, symmetric KH billows growing on a lutocline are documented directly for the first time.

Flow stability is often assessed on basis of the shear magnitude $S = \sqrt{(\partial u/\partial z)^2 + (\partial v/\partial z)^2}$, where u and v are the components of the mean horizontal current and z is the vertical coordinate, the buoyancy frequency $N = \sqrt{-g\partial(\ln\rho)/\partial z}$, where g is the gravitational acceleration and ρ is the net fluid density, and their squared ratio, the gradient Richardson number: $\mathrm{Ri} = N^2/S^2$. $\mathrm{Ri} = 0.25$ is a threshold for shear instability on an inviscid, nondiffusive, steady, parallel mean flow (Miles, 1961). In forced shear flows it is common to observe a state of marginal instability, in which Ri fluctuates around 0.25 as the instability grows, breaks, and decays repeatedly (e.g. Geyer & Smith, 1987; Smyth et al., 2019). In the macrotidal estuary described here, Ri varies with the tide, becoming too large to permit instability at low tide and too small for coherent billows to be detectable at high tide. KH billows are observed primarily as Ri passes through an intermediate range. A more direct approach is to use the solutions of the Taylor-Goldstein equation, or its viscous, diffusive extension, based on observed velocity and density profiles to predict the occurrence and properties of shear instability (Liu et al., 2012; Tedford et al., 2009).

In section 2 we describe our observational methods. Results are described in section 3 and discussed in the context of existing knowledge and research questions in section 4. The main conclusions are summarized in section 5.

2. Data and Methods

Field measurements were carried out in the Jiaojiang River Estuary, southeastern China (Figure 1). The site is shallow with depth ranging between 1 and 3 m at low tide. This macrotidal estuary is dominated by the semidiurnal tide with a maximum range of 6.3 m. Depth-averaged current speed can reach up to 2 m s^{-1}. The bed sediments consist mainly of clay and fine silt with mean grain size slightly less than 8 μm. The estuary is highly turbid, with maximum suspended sediment concentration (SSC) exceeding 40 kg m^{-3} at spring tide (Guan et al., 1998).

A 27-hr in situ observation was conducted between 15:00 (local time), 17 March 2016 and 18:00, 18 March 2016 in the Jiaojiang River Estuary (Figure 1). Ship-borne measurements were carried out at the anchor station (red triangle) to collect velocity and echosounder data. The velocities were measured with a Flowquest 600 kHz acoustic Doppler current profiler (ADCP) sampling at 0.5 Hz and recording an average over 60 s to remove high-frequency variability, with a vertical bin size of 0.5 m. Velocity data within the near-bed region (~0.07H, where H is the water depth, Nystrom et al., 2007) are affected by sidelobe interference and are not used in further analysis. Although 600 kHz ADCP has been confirmed valid in current measurements in high SSC environments (Becker et al., 2018), the ADCP velocity records can be biased by spikes due to high SSC (Cao et al., 2012), which is the case in this study. Hence, a 11-min moving average filter was applied to the ADCP velocity profiles to remove the spikes, similar to that of Becker et al. (2018). An Odom dual echosounder (24/200) kHz was deployed on side of the vessel at 1 m under the sea surface to measure water depth and collect echosounder images, with a sampling rate of 16 Hz and a vertical resolution of 12.5 mm. Unfortunately, echosounder data were missing from 21:18, 17 March to 00:19, 18 March due to power failure.

Hourly profiles of salinity, temperature, and turbidity were obtained using an Idronaut 304 plus CTD with a built-in OBS 3+ sensor sampling at 1 Hz. Water samples were collected at upper (~0.1*H*), intermediate (~0.5*H*), and lower water column (~0.9*H*) using a pump-sampling system. During most of the observation period, the echosounder was deployed on the opposite side of the 4-m-wide vessel from ADCP/CTD, resulting in phase shift and decorrelation between the acoustic and velocity/density profile data (Geyer et al., 2010). However, similar billow structures were observed at both sensor locations, suggesting that the vertical structures of velocity and density generally represent the background flow conditions for the billows.

A Hydrolab DS5 multiparameter Data Sonde collocated with CTD was profiled on a load bearing data cable that provided monitoring of conductivity, temperature, and depth. The real-time data allowed us to avoid direct contact of the instrument with the bottom. The collected water/suspended sediment samples were filtered in the field, and the filters were returned to the laboratory to determine SSC. Based on these samples, we were able to convert the OBS output signals to SSC. The OBS output (Volts) was found to increase with increasing SSC at relatively low range (<8.2 g L^{-1}) and decrease with SSC at high range (>8.2 g L^{-1}). The conversion procedure from OBS volts to SSC was carried out following Kineke and Sternberg (1992). After a process of trial and error, two curves were selected for the low and high SSC ranges, respectively.

$$\ln(OBS) = 0.7\ln(SSC) + 0.02 \qquad SSC < 8.2\ \mathrm{g\ L^{-1}}, \tag{1}$$

$$\ln(OBS) = -5.6\ln(SSC) + 13.3 \qquad SSC > 8.2\ \mathrm{g\ L^{-1}}. \tag{2}$$

Potential sources of error include sampling and weighing errors, contamination from water tubes, and dirty OBS in fluid mud. These errors, as pointed out by Kineke and Sternberg (1992), are difficult to estimate. In spite of these potential errors, the agreements between the data and fitted curves are fairly good ($n = 76$ and $r^2 = 0.92$ for equation (1), $n = 5$ and $r^2 = 0.93$ for equation (2), where n is the number of data points).

Seawater density ρ_{sw} was calculated using the measured temperature and salinity from the CTD. The net density ρ of the sediment-water mixture was calculated using the SSC (e.g., Wright et al., 1986): $\rho = \rho_{sw}(1 - SSC/\rho_s)+SSC$, where $\rho_s = 2{,}650$ g L^{-1} is the sediment density. Density measurements based on CTD profiles were averaged over the same depth intervals as the ADCP (0.5-m intervals). The density and velocity data were then used to calculate buoyancy frequency, shear, and gradient Richardson number.

3. Results

3.1. Intratidal Variations in Hydrographic Structure

Figure 2 shows time series of vertical structures in water velocity, salinity, and SSC at the anchor site. The peak currents were stronger in flood (1.24 m s^{-1}) than in ebb (0.82 m s^{-1}). The tidal current resulted in intense shear in the near-bed region during peak floods and peak ebbs (Figure 2d). The water was well mixed vertically at flood and more saline stratified during ebb, due to tidal straining (Figure 2c), a process that commonly occurs in regions of freshwater influence (Simpson et al., 1990).

Vertical gradients in SSC were stronger at ebb than at flood, especially at late ebb. This is due to the flood-ebb asymmetry in mixing (Lian & Liu, 2015; Simpson et al., 1990; Tu et al., 2019). During the flood tide, sediment tends to be resuspended by strong current and then mixed into the upper water column (e.g., −2 hr relative to second high water [referred to as HW hereafter] in Figure 2b), resulting in relatively homogeneous SSC profiles (Figure 2e). At ebb tide, the weaker current and stronger saline stratification conditions favor weaker turbulence, sediment settling, and hence the formation of concentrated benthic suspension near the bed. As a result, vertical mixing was suppressed and the suspended sediments were concentrated in

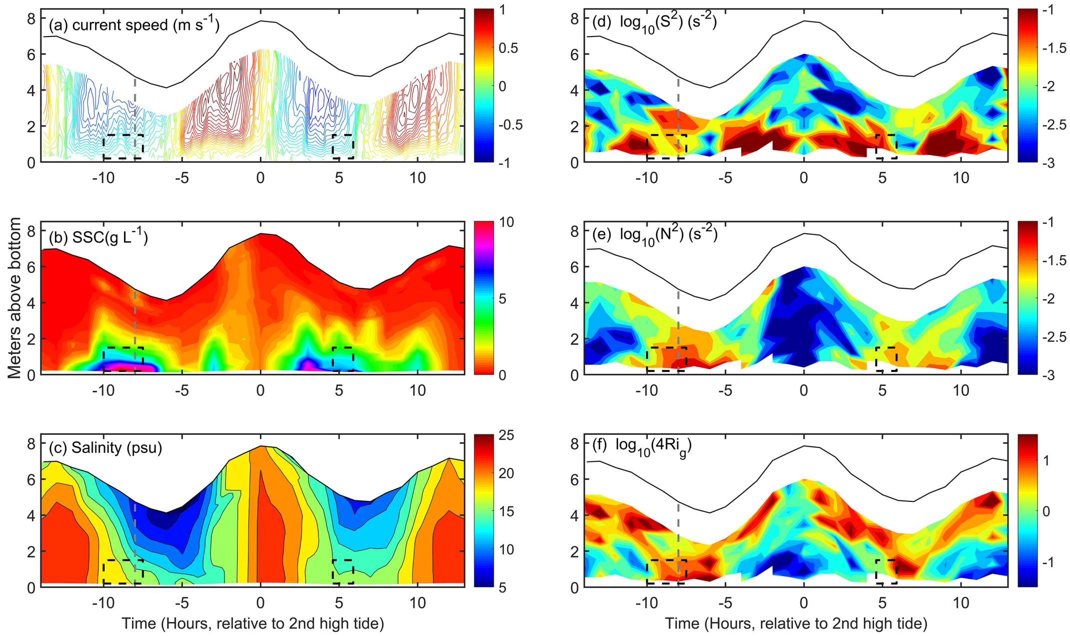

Figure 2. Depth-time variations of (a) velocity (positive upstream), (b) SSC, (c) salinity, logarithm of (d) velocity shear squared, (e) buoyancy frequency squared, and (f) Richardson number (times 4). Boxes represent the periods and vertical range in which the billows have been observed.

the near-bed region. The alternation between occurrence of fluid mud at ebb tide and collapse during flood was consistent with previous observations in the Jiaojiang Estuary (Li et al., 1993) and coincides with the alternation between the occurrence and vanishing of KH billows in our echosounder images.

3.2. Internal Waves and Instabilities

Acoustic imagery has been successfully used to detect wavelike structures that are the finite-amplitude manifestation of instability in the stratified ocean interior (Chang et al., 2016; Moum et al., 2003) and in salt-stratified estuaries (Geyer et al., 2010; Tedford et al., 2009). In this study, echosounder images reveal trains of internal waves and shear instability waves in the near-bed regions within the Jiaojiang Estuary during ebb tides (Figure 2, periods of HW-10 ~ HW-7.5 and HW+4.6 ~ HW+5.9). Echosounder data were missing between HW-7.5 and HW-4.7 due to power failure. However, the echosounder image from HW-4.7 revealed some small billows near-bed, suggesting that instabilities may have persisted during the period without data.

Weather conditions were calm, and no surface waves were present. In addition, no bedforms were observed at the survey site. Hence, the formation mechanism of the observed billows was not likely related to surface waves or to bedforms as described in Trowbridge and Traykovski (2015) and Tedford et al. (2009), respectively. Instead, we believe that the instabilities were produced by the interaction between sediment stratification and current shear. As the CTD and OBS profiling were conducted hourly, the following analyses focus on HW-11, HW-10, HW-9, and HW-8 to investigate temporal evolution of density and velocity structure, and echosounder signal.

The temporal evolution of the instabilities, as well as the flow and density fields, are presented in Figure 3.

- At HW-11, while no instabilities were evident in the echosounder images, signal enhancement was evident around 1 mab (Figure 3a$_1$). Both the velocity and SSC profiles exhibited strong vertical gradients in the near-bed region of 0.8–1 mab (Figures 3b$_1$ and 3c$_1$, gray bands). The salinity gradient was significant in the upper half of the water column but negligible lower down, indicating the dominant contribution of suspended sediment to the near-bed density gradient. The squared buoyancy frequency of the water-sediment mixture near the bed reached values up to 3×10^{-2} s^{-2}, while the maximum shear squared could be higher by a factor 4 or more, yielding Ri slightly smaller than 0.25 at the lower water

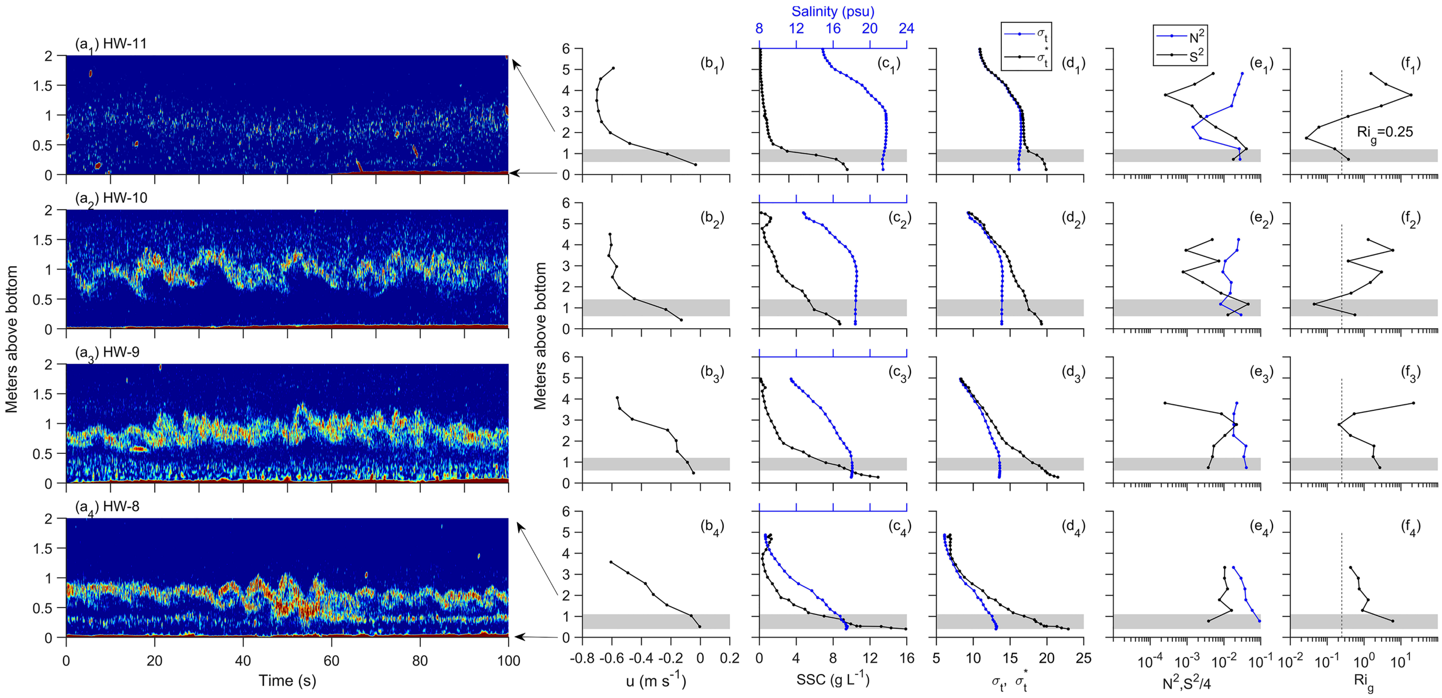

Figure 3. (a) Echosounder image and profiles of (b) velocity, (c) salinity and SSC, (d) densities of water ($\sigma_t = \rho_{sw} - 1{,}000$) and water-sediment mixture ($\sigma_t^* = \rho_m - 1{,}000$), (e) velocity shear squared and buoyancy frequency squared, and (f) gradient Richardson number, for different periods (i.e., HW-11, HW-10, HW-9, and HW-8). Shading indicates depth range of maximum echosounder signal.

column, a condition favorable for the formation of shear instability. The smallest Ri was found above the stratified shear layer; hence, any incipient instability would have been asymmetric.

- At HW-10, wavelike billows were clearly present in the echosounder images as expected (Figure 3a$_2$), indicating that the billows emerged between HW-11 and HW-10. The billows have rounded crests but display sharp cusps on their troughs, similar to the asymmetric Holmboe instabilities described by Carpenter et al. (2007). Despite this resemblance, the Holmboe mechanism is unlikely to be active owing to the lack of a nearby stratified layer; instead, the shear maximum coincides with a minimum in N^2. In this respect the mean flow resembles the model for Taylor instability (e.g., Lee & Caulfield, 2001), a slight variant that would be indistinguishable from KH instability in these observations. The vertical gradients of velocity and SSC decreased compared to those at HW-11, while salinity structure remained similar to that of HW-11 albeit with lower values. Again, the density structure was more SSC dominated closer to the bed compared to the upper water column. S^2 exceeded N^2 while Ri varied around 0.25.
- At HW-9, the echosounder signal was enhanced and revealed a combination of wavelike motions and smaller-scale turbulence. Near-bed shear decreased while SSC and SSC gradient increased, resulting in high N^2, low S^2, and high Ri values. The surface salinity dropped rapidly, leading to high saline gradient in mid-upper water column. In the near-bed region, the salinity remained high and vertically uniform, indicating that the density gradient at this region was dominated by SSC.
- At HW-8, salinity gradient was obvious throughout the water column with a surface-bottom difference of 10 psu, indicating that saline contribution to density stratification became non-negligible (though sediment remained the dominant stratifying agent). Billows were fully turbulent with clear braid-core structures typical of KH instabilities (e.g., Geyer et al., 2010). Unlike those observed at HW-10, these billows are symmetric, with cusps at both crest and trough. Near-bed SSC continued to increase, as did the velocity shear, while Ri still exceeded 0.25. This is counterintuitive as billows generally occur when Ri < 0.25. This inconsistency will be discussed in section 4.1.

Temporal evolution of shear instability has been documented in many previous studies (e.g., Scarlatos & Mehta, 1993; van Haren & Gostiaux, 2010). Thorpe (1987) sketched several stages of KH roll-up and levels of turbulence in lab experiments, controlled by flow conditions including the details of mean shear and

Table 1
Field Observations of Shear Instabilities

Locale	Reference	Measurement	Figure	Symmetry	Height/depth	Wavelength	Amplitude	Aspect ratio
Thermohaline stratification: Ocean								
Equatorial Pacific	Hebert et al. (1992)	u,v,T,S (no ES)	3a	A	−50/4,000	150	25	0.17
Romanche Fracture Zone	van Haren et al. (2014)	u,v,T,S (no ES)	3, 4	A	200/4,700	700?	100?	0.14
Kuroshio, Northwestern Pacific	Chang et al. (2016)	ES, u,v,T,S, microstructure	2	S	50/230	225	70	0.31
Cont. shelf, Oregon	Moum et al. (2003)	ES, u,v,T,S	14	S	−20/100	80	12	0.14
Admiralty Inlet, USA	Seim and Gregg (1994)	ES, u,v,T,S, microstructure	P1, 5	A	70/120	75	15	0.20
Thermohaline stratification: Estuarine								
Fraser R., Canada	Geyer and Smith (1987)	ES, u,v,S,T	6	S	6/14	9	1	0.11
St. Lawrence, R., Canada	Bourgault et al. (2001)	ES, u,v,S,T	7c	A	50/75	151	10	0.07
Fraser R., Canada	Tedford et al. (2009)	ES, u,v,S,T	3a	S	7/14	55	5	0.09
			3b	A	6/16	20	1.5	0.08
			3c	S	4/12	35	3	0.09
Connecticut R., USA	Geyer et al. (2010)	ES, u,v,T,S	3a, 4a	S	4.5/7	5–10	1.5	0.15–0.30
		microstructure	3b, 4b	S	4/7	10	1.5	0.14
Connecticut R., USA	Geyer et al. (2017)	ES, u,v,T,S	3	S	5.5/8	30	3	0.10
Sediment stratification								
Ems R., Germany	Held et al. (2019, 2013)	Sediment ES, u,v,S,T, SSC	3c	A	4/10	2.4 ± 0.5	1	0.34–0.53
Namyang Bay, South Korea	Adams et al. (1990)	Surface photo u,v, transparency	3, 4	n/a	2/4	5	n/a	n/a
Jiaojiang R., China	Jiang and Wolanski (1998)	Acoustic image	3, 4	A		1.3 ± 0.5	0.5	0.28–0.62
Jiaojiang R., China	Present study	ES, u,v,T,S, SSC	$3a_2$	A	1/5.5	3.6	0.5	0.14
			$3a_4$, 4	S	0.7/5	1.2	0.7	0.58

Note. Columns are (1) study area, (2) study referenced, (3) measurements used (ES = echosounder), (4) figure referenced, (5) symmetry of instability (S = symmetric; A = asymmetric), (6) height above the bottom and total water depth (m, negative values are measured from surface), (7) estimated wavelength (m), (8) estimated amplitude (m), and (9) aspect ratio (height/wavelength).

stratification during instability growth (van Haren & Gostiaux, 2010). At these stages, wavelike KH instabilities form, roll up into billows connected by braids, and become fully turbulent. Secondary billows may form on the braids and in the peripheries of the cores (Figure 7 of van Haren & Gostiaux, 2010; Salehipour et al., 2015). This is consistent with instability evolution found in the stratified fluid mud/water interface (Figure 6 of Scarlatos & Mehta, 1993).

KH-like billows have been observed in the open ocean, in thermohaline-stratified estuaries, and on near-bed lutoclines. Here we compare observations in terms of symmetry, wavelength, amplitude, and aspect ratio based on published data (Table 1). Most observations were via echosounder images, but Hebert et al. (1992) and van Haren et al. (2014) were able to image the time-depth structure using high-resolution temperature profiles with similar results. The distinction between symmetric and asymmetric billows is subjective but is generally clear in practice. Symmetric billows indicate that localized layers of strong shear and stratification coincide closely, as might be expected in a two-layer flow. While this ideal state is not found in nature, it is often approximated closely enough to produce symmetric-looking billows (Table 1, column 5). In most cases, wavelength was estimated by multiplying the period shown by the echosounder with the velocity at the depth of maximum shear (representing the phase velocity, e.g., Smyth et al., 2011). In the present observations, the wavelength of billows varied between ~1 and 4 m (Figures 3b, 3d, and 4c and Table 1). Taking the vertical distance between the trough and peak, the height of the instability ranges from approximately 0.2 to 0.7 m.

In flow of the Kuroshio over a seamount, Chang et al. (2016) reported billows with size two decades larger than we see here, and billows on a similarly gargantuan scale have been reported in the abyssal ocean by van Haren et al. (2014). While observed wavelengths and amplitudes range over 2 orders of magnitude (Table 1, columns 7 and 8), the aspect ratio (height/wavelength, Table 1, column 9) is relatively consistent. In the

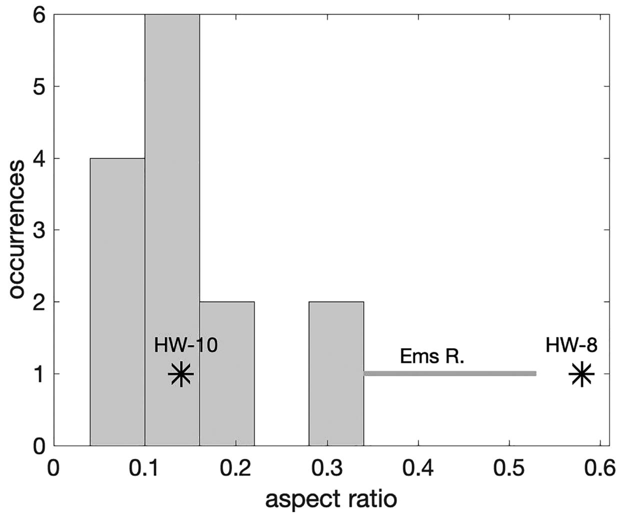

Figure 4. Histogram of aspect ratio from oceanic and estuarine observations of shear instability. The gray line is our estimate of the uncertainty range for asymmetric billows observed on the Ems Estuary (Held et al., 2019). Asterisks represent the current measurements (cf. Figure 3).

thermohaline cases, the mean aspect ratio is 0.15 and the standard deviation is 0.08. While the uncertainty is large, especially for wavelength estimates, the available data suggest that the lutocline cases may have relatively high aspect ratio (height/wavelength; Figure 4). In terms of aspect ratio, the symmetric disturbances shown in Figures 3a$_4$and 5a–5c are "tall" in comparison with most other observations (Table 1, final column). The same is true of the features observed in the Ems Estuary (Figure 4, gray line). This could be an artifact due to the difficulty of measuring the velocity (and hence the wavelength) this close to the bottom in sediment-laden fluid. Just as plausibly, it could be a signal that the physics of the instability and its evolution to large amplitude changes in proximity to the boundary. For example, in the lab experiments of Thorpe (1973), large aspect ratio is associated with small Ri, as might be expected in the strongly sheared flow near the boundary.

A 9-min echosounder image near HW-8 reveals several packets, each consisting of several billows (Figure 5a). A close-up of the image reveals a group of unstable waves growing and decaying temporally (Figure 5b). The structure of the billows presented in Figure 5c is in good agreement with those from previous observations and numerical simulations, but with smaller scale, possibly due to the proximity of the benthic boundary. A detailed view of the instabilities reveals the familiar structure consisting of braid and core, resembling those in echosounder images of KH instabilities reported previously (Geyer et al., 2010; Tedford et al., 2009). We show in Figure 5 successively more detailed views of observed billows along with previous observations and a model for comparison. Previous simulation results and echosounder images from a salt-stratified estuary encourage us to identify the KH instability structures in the present observation, as we now describe. Geyer et al. (2010) observed a similar billow structure in echosounder images with strong echo intensity in the S-shaped braids and weaker intensity in the cores. As Geyer et al. (2010) pointed out, the regions of high backscatter (the braids) represent strong vertical density gradient while weak acoustic return indicates relatively well-mixed fluid (the cores).

As a standard for comparison, we interrogate a direct numerical simulation (DNS) of KH billows with a virtual echosounder (Figure 5e). The DNS is initialized with nondimensional velocity and buoyancy profiles:

$$U(z) = 1 + \tanh(z); \; B(z) = \mathrm{Ri}_0 \tanh(z) \tag{3}$$

plus small-amplitude noise to catalyze the instability. The initial Richardson and Reynolds numbers were $\mathrm{Ri}_0 = 0.16$ and $\mathrm{Re}_0 = 1{,}000$, and the Prandtl number was unity. Further details of the DNS can be found in Kaminski and Smyth (2019) (The constant 1 in the velocity profile (3) was added after the fact via a Galilean transformation of the DNS data.). The squared vertical density gradient was plotted as a proxy for the flow property registered by the echosounder (e.g., Ross et al., 2004). Sequential profiles extracted at a fixed horizontal location were concatenated, simulating the signal detected by an echosounder on a stationary ship as a train of billows passes. In both observations and simulation, the signal is brightest in the braids due to the strong stratification there, and the braids reveal the familiar symmetric, interlocking S-shape.

4. Discussion

4.1. The Miles-Howard Criterion

If molecular effects are negligible and the initial flow is parallel, a necessary (though not sufficient) condition for the flow to become unstable is that the minimum value of Ri be less than 0.25, as shear is then strong enough to work against gravity to initiate vertical motions. Since this result was proven (Howard, 1961; Miles, 1961), experience has shown that Ri < 0.25 is a useful, practical indicator of shear instability under fairly general conditions (Smyth & Carpenter, 2019).

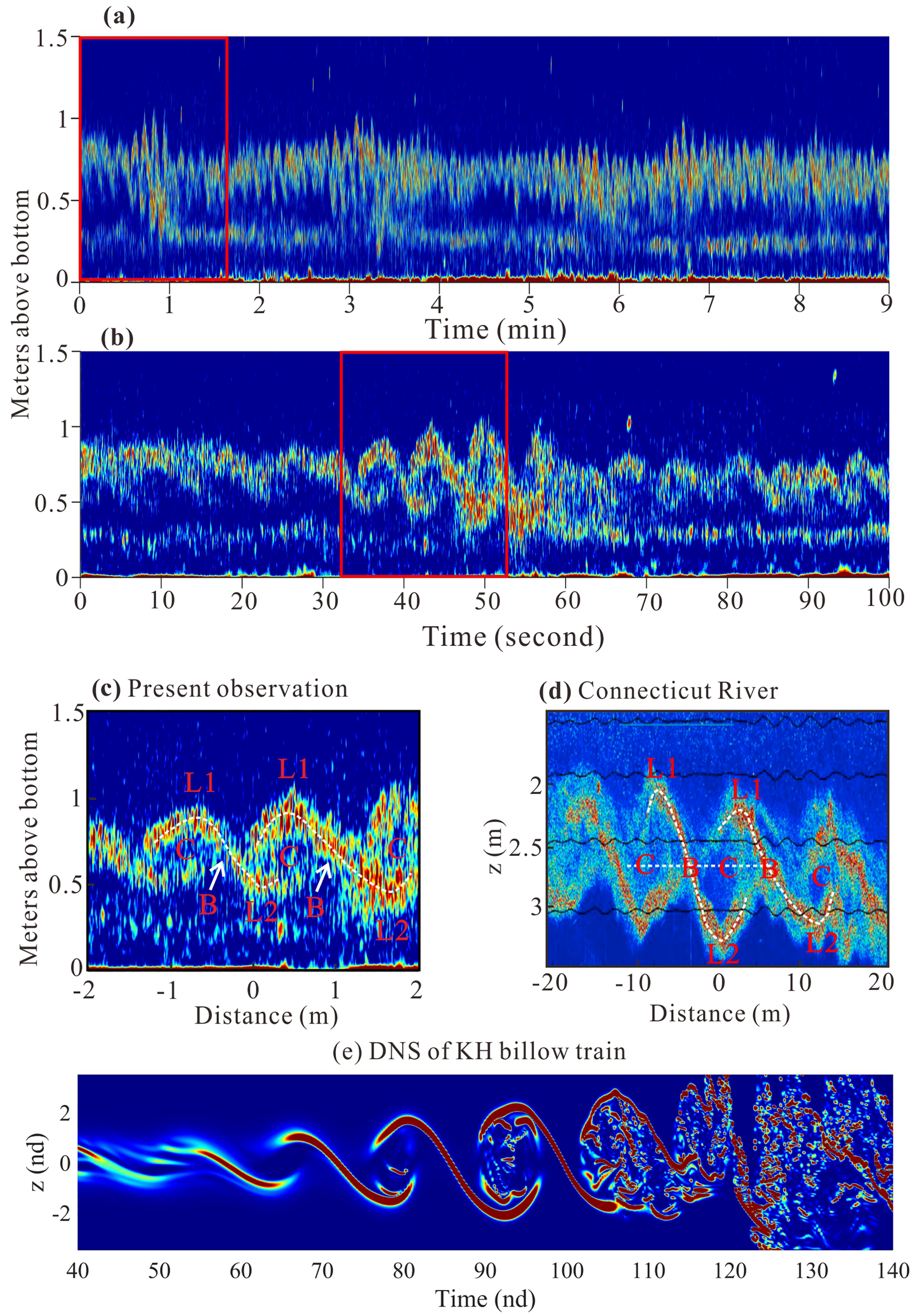

Figure 5. (a) Echosounder image showing successive turbulent events. (b) Detail of a single event from the red box marked in on (a). (c) Detail of individual billows. Labels L1, L2, B, and C represent the upper eyelid, lower eyelid, braid, and core of the KH billows. (d) Echosounder from Connecticut River estuary (Geyer et al., 2010) for comparison. (e) Simulated echosounder signal from a passing KH billow train (modified from Kaminski & Smyth, 2019), showing the classic S-shape with strong signal in the braids.

An important factor that influences measurements of Ri is the spatial and temporal scales at which the shear and stratification are measured. In general, under-resolution leads to overestimation of Ri. Smyth and Moum (2013) showed how the vertical resolution influences the statistics of Ri in the Pacific equatorial undercurrent: Observations of Ri < 0.25 become more frequent with finer resolution and less frequent with coarser resolution. The same is true of temporal resolution: Temporal averaging tends to erase small values of Ri (Pham et al., 2017). Shear instabilities may therefore occur even though the measured estimate of Ri exceeds 0.25. Bourgault et al. (2001) used an Ri range of 0.25 and 0.5 to indicate instability conditions, considering that internal waves, which enhance shear locally, were not resolved by their measurements. Moum et al. (2003) observed KH billows associated with near-surface internal solitary waves while Ri > 1, attributing this to unresolved vertical shears. In the present measurements, because of the 11-min moving average needed to control sediment-induced spiking in ADCP velocity records, the small values of Ri that precede instability are likely to be obscured. In fact, an 11-min period may contain several complete episodes of instability (e.g., Figure 5a).

In the present regime, Ri varies on two important time scales. First is the tidal cycle: Ri varies between values close to 0 (at high water) and greater than 0.25 (at low water). In the latter case, instability is rare for the reasons discussed above. In the former case, stratification is so weak as to be nearly irrelevant. At the flood tide (i.e., periods from low tide to high tide), strong, small-scale, and isotropic turbulence is likely to dominate due to the effect of tidal straining, which tends to enhance turbulent mixing at flood and stratifies the water at ebb. Moreover, any coherent billows that may exist are unlikely to register on the echosounder because they carry only weak density contrasts (also see Tedford et al., 2009). At ebb tide, the water column is stratified by both salt (upper water column) and suspended sediment (lower water column). The formation of fluid mud layer at the near-bed region interacts with current shear, favoring the occurrence of billows. Therefore, billows are most likely to appear during the transitional times at ebb tide, when Ri is less than 0.25 but greater than some small value $\mathrm{Ri}_{\mathrm{min}}$ (likely ~0.1 or less). In addition, lateral expansion of the channel (Figure 1) might contribute to the active shear instability at ebb. The conservation of angular momentum intensifies shear, lowering Ri and thereby promoting instability (Chant & Wilson, 2000; Geyer et al., 2017). The effect is reversed at flood tide, partially explaining why billows are observed at ebb but not at flood.

The second important time scale is associated with "marginal instability," the threshold behavior described by Geyer and Smith (1987) and discussed recently by Thorpe and Liu (2009), Smyth and Moum (2013), Geyer et al. (2017), and Smyth et al. (2013, 2019, 2017). A slowly varying external force, here supplied by the tide acting against bottom friction, accelerates the shear and thus decreases Ri until it drops below 0.25. Instabilities then grow and become turbulent. Turbulent mixing reverses the decrease of Ri, eventually resulting in Ri > 0.25. Turbulence then decays, but meanwhile the external force reaccelerates the flow and the cycle repeats (see Smyth et al., 2019, for a more detailed description). The second time scale is only a few minutes. Three such cycles are visible in Figure 5a, with strong turbulence visible near t = 1, 3, and 6–7 min.

4.2. Comparison With Linear Stability Analysis

Stability is assessed theoretically by considering the evolution of a small perturbation on a steady, parallel shear flow. We assume that each perturbation field has the normal mode form, for example,

$$w' = \{\hat{w}(z)exp[i(kx + ly - \omega t)]\}_r, \tag{4}$$

where w' is the vertical velocity (or any other perturbation field), $\hat{w}(z)$ is a complex amplitude function to be determined, (k,l) is a real horizontal wave vector with components in the Cartesian directions x and y, and $\omega = \omega_r + i\omega_i$ is a complex frequency. The subscript r denotes the real part. If $\omega_i > 0$, the disturbance grows exponentially.

For the present calculations we neglect viscosity and diffusivity, so that the theory is equivalent to the well-known Taylor-Goldstein equation (e.g., Smyth et al., 2011). We assume impermeable, fixed density boundaries at $z = 0$ and $z = 4.5$ m. (Auxiliary calculations including viscosity and a no-slip condition at $z = 0$ give substantially the same result.) The equations are discretized via the Fourier-Galerkin method (e.g. Lian et al., 2020).

Profiles at HW-10 reveal a region surrounding $z = 1$ m where the shear reaches a maximum and stratification is a minimum such that Ri < 1/4, ideal conditions for shear instability (Figures 6a and 6b). We scan the $k - l$ plane in polar form, where $\kappa = \sqrt{k^2 + l^2}$ and $\theta = \tan^{-1}(l/k)$. We find that the fastest-growing mode has growth rate $\omega_i = 0.061\ \mathrm{s}^{-1}$. The billows shown in Figures 3 and 5 evolve on a time scale of a few minutes, while the predicted instability grows by a factor e in about 16 s, showing that the instability could easily emerge and reach macroscopic amplitude over the observed time scale. The vertical displacement

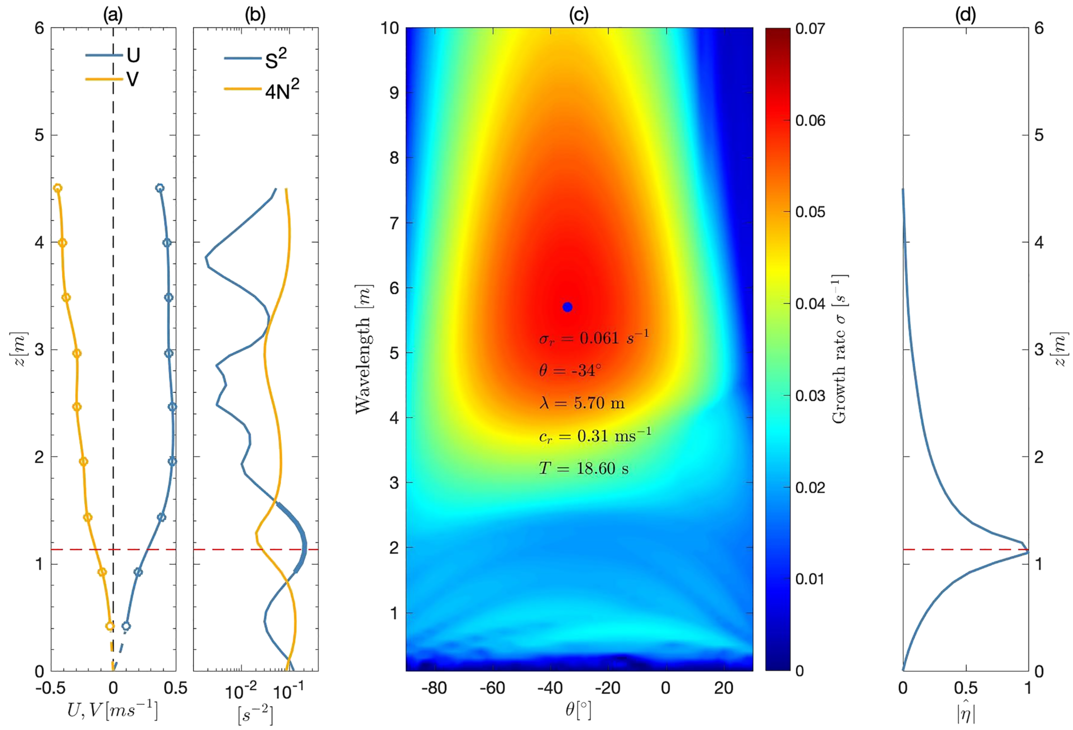

Figure 6. Solutions of the Taylor-Goldstein equation based on velocity and density profiles observed at HW-10. (a) Velocity components, both original (circles) and spline-interpolated, interpolated to the bottom (dashed) assuming $u = v = 0$ at $z = 0$. (b) Squared shear and $4N^2$. The factor 4 makes it easy to see when Ri < 1/4 (thick part of blue curve). (c) Growth rate versus wavelength and orientation angle (counterclockwise from eastward). Annotations are properties of the fastest-growing mode. (d) Vertical displacement eigenfunction $\hat{\eta} = -i\hat{w}/k(U - c)$. Horizontal dashed lines show the critical level, where $U(z_c) = c$.

eigenfunction $\hat{\eta}$ is a maximum near $z = 1$ m, consistent with the echosounder image. The predicted billows have wavelength 5.7 m and phase speed 0.31 m s^{-1}, directed at 31° south of east, similar to the direction of the current (Figure 6a) and slightly to the right of the channel orientation (Figure 1).

The predicted period is 19 s, longer by a factor 2 than that of the oscillations shown in Figure 3a$_2$. We believe that this discrepancy results from under-resolution. The apparent thickness of the shear layer is of order 1 m, so its detailed structure is not well resolved by our 0.5-m ADCP measurements. Suppose the shear layer was in fact only 0.5 m thick, a difference that our current measurements would not register. It would produce an instability with half the period we compute, consistent with the echosounder image (Figure 3a$_2$).

4.3. Implications for Sediment Transport in Hyperturbid Systems

To our knowledge, this is the first definitive identification of KH instabilities induced by the interaction between shear and sediment-induced stratification in a natural estuary. In a flume experiment, Scarlatos and Mehta (1993) observed the presence of KH billows along the interface between fluid mud and the overlying water. Shear instability was thought to play a significant role in the erosion of the fluid mud (Scarlatos & Mehta, 1990). They successfully reproduced the interfacial instabilities using numerical simulations. Such instabilities are very likely to contribute to the entrainment of fluid mud into upper fluid (Scarlatos & Mehta, 1993). Held et al. (2013) and Held et al. (2019) pointed out that internal waves breaking associated with shear instability mixes sediment-laden fluid mud into the upper water layer. The layer with shear instabilities is typically more turbulent than the water above and below, leading to vertical transport of both mass and momentum (e.g., Chang et al., 2016; Geyer et al., 2010). As modeled by Bruens et al. (2011), a turbulent, near-bed region of concentrated benthic suspension is found to entrain overlying water and water and sediment from underlying water. This indicates that shear instabilities might act to mix/entrain sediment between the lower and upper water column, modifying sediment transport patterns in these turbid estuarine waters.

The present study might provide a mechanism for the entrainment of sediment from the fluid mud into the lower and upper layer (e.g., Becker et al., 2018). Lacking microstructure measurements, we have estimated the turbulent mass flux using the billow size revealed in the echosounder images.

Klymak and Legg (2010) proposed parameterizing the turbulent kinetic energy dissipation rate ε as

$$\varepsilon = L_T^2 N^3, \tag{5}$$

in which L_T is the Thorpe scale, a measure of the root-mean-square vertical displacement of water parcels. Based on this, the Osborn (1980) method may be used to estimate the turbulent buoyancy flux as $\Gamma\varepsilon$, where the coefficient Γ is approximated by 0.2. Equivalently, the turbulent mass flux is

$$J_\rho = \Gamma L_T^2 N^3 \frac{\rho}{g}. \tag{6}$$

The present observations cannot tell us L_T, but we are able to quantify the height of the billows by visually examining the echosounder images and measuring the vertical distance between the uppermost and lowermost regions of strong signal. We call this height h_{ES}. In Figure 5c, for example, h_{ES} is approximately 0.5 m. To estimate the turbulent density flux, we define a coefficient that relates the two lengths, $C = (L_T/h_{ES})^2$, after which the density flux is

$$J_\rho = C\Gamma h_{ES}^2 N^3 \frac{\rho}{g}. \tag{7}$$

As a first guess for C, we note that h_{ES} should be similar to the "patch height" L_p as defined for turbulent patches in microstructure profiles (Moum, 1996). Examining both microstructure observations and direct simulations of KH billows, Smyth et al. (2001) found values of L_p/L_T between 2 and 20, with smaller values corresponding to the "young" events that show up on the echosounder (their Figure 4a). Here, we will make the conservative choice $L_p/L_T = 10$, hence, $C = 0.01$, noting that this may be an underestimate. Inserting $h_{ES} \approx 0.5$ m, $N^2 \approx 0.1$ s^{-1} (based on Figure 4e$_4$), $\rho \approx 1{,}000$ kg m^{-3}, and $g \approx 10$ m s^{-2} into (7), we obtain a mass flux per unit area of 1.6×10^{-3} kg s^{-1} m^{-2}.

If this flux is applied 1 m above the bottom, and there is no flux at the bottom, the resulting density loss in the bottom meter is1.6×10^{-3} kg s^{-1} m^{-2}. As is evident in Figure 3c, a typical suspended sediment load is 10 g L^{-1}(or kg m^{-3}), so the time needed for this mass flux to erase it completely is 6.25×10^3 s, or 1.7 hr. This is only an order of magnitude estimate, but it suggests that the turbulent mass flux due to the instabilities revealed by the echosounder, acting over a few hours, is sufficient to significantly alter the suspended sediment distribution.

We conclude that the observed shear instabilities act to counter the effect of suspended sediment-induced stratification with a time scale of a few hours, modifying the intratidal sediment transport patterns. In particular, the offshore sediment transport might be enhanced given that the active KH billows were observed during ebb phases. Detailed turbulence measurements are needed to resolve the mixing processes within the spatial structure of the instability and their impact on sediment suspension and transport.

5. Conclusions

Working in a tidally dominated estuary with a dense fluid mud layer on the bottom, we have analyzed echosounder images together with vertical profiles of velocity, temperature, salinity, and SSC. The main findings are summarized as follows:

- Symmetric KH billows growing on a lutocline have been observed directly for the first time. The echosounder signal resembles synthetic images from a DNS of a KH billow train.
- Asymmetric billows appearing earlier in the ebb tide are well predicted by linear instability theory.
- The ebb-flood asymmetry in instability occurrence is consistent with the expected effects of tidal straining and with the seaward expansion of the channel.

- The KH billows have the potential to modify estuarine sediment transport processes. The threshold behavior of KH instabilities in a forced system is evident during ebb tide, when Ri transitions from 0.25 to ~0.1.

It is worth noting that density gradients in KH billows are not just a proxy for the echosounder signal; they are a fundamental measure of mixing (Winters & D'Asaro, 1996) and are therefore an important target for future investigation. Future work should also focus on the influence of the nearby boundary on the evolution of the KH instability and the resulting mixing processes.

Acknowledgments
The contribution of J. Tu, D. Fan, and W. Liu was with the support of the National Natural Science Foundation of China (41776052), the Laboratory of Marine Geology, Qingdao National Laboratory for Marine Science and Technology (MGQNLM-TD201802), and the Research Fund of State Key Laboratory of Marine Geology in Tongji University (MG20190104). J. Tu was also supported by China Postdoctoral Science Foundation (2018 M642072) and the National Natural Science Foundation of China (41906052). Q. Lian and Z. Liu were supported by the National Natural Science Foundation of China (41622601, 91858201, and 41721005) and the National Key R&D Program of China (2016YFC1401404). The participation of A. Kaminski and W. Smyth was supported by the U.S. National Science Foundation under Grant OCE-1537173. The data are publicly available (at https://zenodo.org/record/3547927#.XdSU1egzaUl) and can also be found in supporting information to this manuscript.

References

Adams, C. E. Jr., Wells, J. T., & Park, Y.-A. (1990). Internal hydraulics of a sediment-stratified channel flow. *Marine Geology*, *95*(2), 131–145.

Becker, M., Maushake, C., & Winter, C. (2018). Observations of mud-induced periodic stratification in a hyperturbid estuary. *Geophysical Research Letters*, *45*(11), 5461–5469. https://doi.org/10.1029/2018GL077966

Bourgault, D., Saucier, F. J., & Lin, C. A. (2001). Shear instability in the St. Lawrence Estuary, Canada: A comparison of fine-scale observations and estuarine circulation model results. *Journal of Geophysical Research: Oceans*, *106*(C5), 9393–9409.

Bruens, A., Winterwerp, J., & Kranenburg, C. (2011). Physical and numerical modeling of the entrainment by a high-concentration mud suspension. *Journal of Hydraulic Engineering*, *138*(6), 479–490.

Cao, Z., Wang, X. H., Guan, W., Hamilton, L. J., Chen, Q., & Zhu, D. (2012). Observations of Nepheloid layers in the Yangtze Estuary, China, through phase-corrupted acoustic Doppler current profiler speeds. *Marine Technology Society Journal*, *46*(4), 60–70. https://doi.org/10.4031/MTSJ.46.4.6

Carpenter, J. R., Balmforth, N. J., & Lawrence, G. A. (2010). Identifying unstable modes in stratified shear layers. *Physics of Fluids*, *22*(5), 054104.

Carpenter, J. R., Lawrence, G. A., & Smyth, W. D. (2007). Evolution and mixing of asymmetric Holmboe instabilities. *Journal of Fluid Mechanics*, *582*, 103–132. https://doi.org/10.1017/S0022112007005988

Chang, M. H., Jheng, S. Y., & Lien, R. C. (2016). Trains of large Kelvin-Helmholtz billows observed in the Kuroshio above a seamount. *Geophysical Research Letters*, *43*(16), 8654–8661.

Chant, R. J., & Wilson, R. E. (2000). Internal hydraulics and mixing in a highly stratified estuary. *Journal of Geophysical Research: Oceans*, *105*(C6), 14,215–14,222.

Geyer, W. R., Lavery, A. C., Scully, M. E., & Trowbridge, J. H. (2010). Mixing by shear instability at high Reynolds number. *Geophysical Research Letters*, *37*(22).

Geyer, W. R., Ralston, D. K., & Holleman, R. C. (2017). Hydraulics and mixing in a laterally divergent channel of a highly stratified estuary. *Journal of Geophysical Research: Oceans*, *122*(6), 4743–4760. https://doi.org/10.1002/2016jc012455

Geyer, W. R., & Smith, J. D. (1987). Shear instability in a highly stratified estuary. *Journal of Physical Oceanography*, *17*(10), 1668–1679.

Guan, W. B., Wolanski, E., & Dong, L. X. (1998). Cohesive sediment transport in the Jiaojiang River estuary, China. *Estuarine, Coastal and Shelf Science*, *46*(6), 861–871.

Hebert, D., Moum, J. N., Paulson, C. A., & Caldwell, D. R. (1992). Turbulence and internal waves at the equator. Part II: Details of a single event. *Journal of Physical Oceanogrraphy*, *22*, 1346–1356.

Held, P., Bartholomä-Schrottke, K., & Bartholomä, A. (2019). Indications for the transition of Kelvin-Helmholtz instabilities into propagating internal waves in a high turbid estuary and their effect on the stratification stability. *Geo-Marine Letters*, *39*(2), 149–159. https://doi.org/10.1007/s00367-019-00564-4

Held, P., Schrottke, K., & Bartholomä, A. (2013). Generation and evolution of high-frequency internal waves in the Ems estuary, Germany. *Journal of Sea Research*, *78*, 25–35.

Holleman, R. C., Geyer, W. R., & Ralston, D. K. (2016). Stratified turbulence and mixing efficiency in a salt wedge estuary. *Journal of Physical Oceanography*, *46*, 1769–1783.

Howard, L. N. (1961). Note on a paper of John W. Miles. *Journal of Fluid Mechanics*, *10*(4), 509–512.

Jiang, J., & Wolanski, E. (1998). Vertical mixing by internal wave breaking at the lutocline, Jiaojiang River estuary, China. *Journal of Coastal Research*, *14*, 1426–1431.

Kaminski, A., & Smyth, W. (2019). Stratified shear instability in a field of pre-existing turbulence. *Journal of Fluid Mechanics*, *862*, 639–658.

Kineke, G., & Sternberg, R. (1992). Measurements of high concentration suspended sediments using the optical backscatterance sensor. *Marine Geology*, *108*(3–4), 253–258.

Kirby, R., & Parker, W. (1983). Distribution and behavior of fine sediment in the Severn Estuary and Inner Bristol Channel, UK. *Canadian Journal of Fisheries and Aquatic Sciences*, *40*(S1), s83–s95.

Klymak, J., & Legg, S. (2010). A simple mixing scheme for models that resolve breaking internal waves. *Ocean Model*, *33*, 224–234.

Lavery, A. C., Geyer, W. R., & Scully, M. E. (2013). Broadband acoustic quantification of stratified turbulence. *The Journal of the Acoustical Society of America*, *134*(1), 40–54.

Lawrence, G. A., Haigh, S. P., & Zhu, Z. (1998). In search of Holmboe's instability. In J. Imberger (Ed.), *Physical processes in lakes and oceans, Coastal and estuarine studies*, (Vol. 54, pp. 295–304). Washington, DC: American Geophysical Union.

Lee, V., & Caulfield, C. (2001). Nonlinear evolution of a layered stratified shear flow. *Dynamics of Atmospheres and Oceans*, *34*, 103–124.

Li, Y., Wolanski, E., & Xie, Q. (1993). Coagulation and settling of suspended sediment in the Jiaojiang River estuary, China. *Journal of coastal Research*, 390–402.

Lian, Q., & Liu, Z. (2015). Turbulence and mixing in a freshwater-influenced tidal bay: Observations and numerical modeling. *Science China: Earth Sciences.*, *58*(11), 2049–2058.

Lian, Q., Smyth, W. D., & Liu, Z. (2020). Numerical computation of instabilities and internal waves from in situ measurements via the viscous Taylor-Goldstein problem. *Journal of Atmospheric and Oceanic Technology*. https://doi.org/10.1175/JTECH-D-19-0155.1

Liu, Z., Thorpe, S., & Smyth, W. (2012). Instability and hydraulics of turbulent stratified shear flows. *Journal of Fluid Mechanics*, *695*, 235–256. https://doi.org/10.1017/jfm.2012.13

Miles, J. W. (1961). On the stability of heterogeneous shear flows. *Journal of Fluid Mechanics*, *10*(4), 496–508.

10.1029/2019JC015383

Moum, J., Farmer, D., Smyth, W., Armi, L., & Vagle, S. (2003). Structure and generation of turbulence at interfaces strained by internal solitary waves propagating shoreward over the continental shelf. *Journal of Physical Oceanography*, *33*(10), 2093–2112.

Moum, J. N. (1996). Energy-containing scales of turbulence in the ocean thermocline. *Journal of Geophysical Research*, *101*(C6), 14,095–14,109.

Nystrom, E. A., Rehmann, C. R., & Oberg, K. A. (2007). Evaluation of mean velocity and turbulence measurements with ADCPs. *Journal of Hydraulic Engineering*, *133*(12), 1310–1318.

Osborn, T. R. (1980). Estimates of the local rate of vertical diffusion from dissipation measurements. *Journal of Physical Oceanography*, *10*, 83–89.

Pham, H. T., Smyth, W. D., Sarkar, S., & Moum, J. N. (2017). Seasonality of deep cycle turbulence in the eastern equatorial Pacific. *Journal of Physical Oceanography*, *47*(9), 2189–2209.

Ross, T., Garrett, C., & Lueck, R. (2004). On the turbulent co-spectrum of two scalars and its effect on acoustic scattering from oceanic turbulence. *Journal of Fluid Mechanics*, *514*, 107–119.

Salehipour, H., Peltier, W., & Mashayek, A. (2015). Turbulent diapycnal mixing in stratified shear flows: The influence of Prandtl number on mixing efficiency and transition at high Reynolds number. *Journal of Fluid Mechanics*, *773*, 178–223. https://doi.org/10.1017/jfm.2015.225

Scarlatos, P. D., & Mehta, A. J. (1990). Some observations on erosion and entrainment of estuarine fluid muds. In R. T. Cheng (Ed.), *Residual currents and long-term transport*, (Vol. 38, pp. 321–332). Berlin: Springer.

Scarlatos, P. D., & Mehta, A. J. (1993). Instability and entrainment mechanisms at the stratified fluid mud-water interface. In A. J. Mehta (Ed.), *Nearshore and estuarine cohesive sediment transport, Coastal and estuarine studies*, (Vol. 42, pp. 205–223). Washington, DC: American Geophysical Union.

Seim, H. E., & Gregg, M. C. (1994). Detailed observations of a naturally occurring shear instability. *Journal of Geophysical Research: Oceans*, *99*(C5), 10,049–10,073.

Simpson, J. H., Brown, J., Matthews, J., & Alen, G. (1990). Tidal straining, density currents, and stirring in the control of estuarine stratification. *Estuaries*, *13*(2), 125–132.

Smyth, W., Moum, J., & Caldwell, D. (2001). The efficiency of mixing in turbulent patches: Inferences from direct simulations and microstructure observations. *Journal of Physical Oceanography*, *31*(8), 1969–1992.

Smyth, W., Moum, J., Li, L., & Thorpe, S. (2013). Diurnal shear instability, the descent of the surface shear layer, and the deep cycle of equatorial turbulence. *Journal of Physical Oceanography*, *43*(11), 2432–2455.

Smyth, W., Nash, J., & Moum, J. (2019). Self-organized criticality in geophysical turbulence. *Scientific Reports*, *9*(1), 3747. https://doi.org/10.1038/s41598-019-39869-w

Smyth, W. D., & Carpenter, J. R. (2019). *Instability in geophysical glows*. Cambridge, England: Cambridge University Press.

Smyth, W. D., & Moum, J. N. (2012). Ocean mixing by Kelvin-Helmholtz instability. *Oceanography*, *25*(2), 140–149.

Smyth, W. D., & Moum, J. N. (2013). Marginal instability and deep cycle turbulence in the eastern equatorial Pacific Ocean. *Geophysical Research Letters*, *40*(23), 6181–6185. https://doi.org/10.1002/2013GL058403

Smyth, W. D., Moum, J. N., & Nash, J. D. (2011). Narrowband, high-frequency oscillations at the equator. Part II: Properties of shear instabilities. *Journal of Physical Oceanography*, *41*, 412–428.

Smyth, W. D., Pham, H. T., Moum, J. N., & Sarkar, S. (2017). Pulsating turbulence in a marginally unstable stratified shear flow. *Journal of Fluid Mechanics*, *822*, 327–341. https://doi.org/10.1017/jfm.2017.283

Tedford, E., Carpenter, J., Pawlowicz, R., Pieters, R., & Lawrence, G. A. (2009). Observation and analysis of shear instability in the Fraser River estuary. *Journal of Geophysical Research: Oceans*, *114*(C11).

Thorpe, S. (1973). Experiments on instability and turbulence in a stratified shear flow. *Journal of Fluid Mechanics*, *61*(4), 731–751.

Thorpe, S. (1987). Transitional phenomena and the development of turbulence in stratified fluids: A review. *Journal of Geophysical Research: Oceans*, *92*(C5), 5231–5248.

Thorpe, S., & Liu, Z. (2009). Marginal instability? *Journal of Physical Oceanography*, *39*(9), 2373–2381.

Trowbridge, J. H., & Traykovski, P. (2015). Coupled dynamics of interfacial waves and bed forms in fluid muds over erodible seabeds in oscillatory flows. *Journal of Geophysical Research: Oceans*, *120*(8), 5698–5709.

Tu, J., Fan, D., Zhang, Y., & Voulgaris, G. (2019). Turbulence, sediment induced stratification, and mixing under macrotidal estuarine conditions (Qiantang Estuary, China). *Journal of Geophysical Research: Oceans.*. https://doi.org/10.1029/2018JC014281

van Haren, H., & Gostiaux, L. (2010). A deep-ocean Kelvin-Helmholtz billow train. *Geophysical Research Letters*, *37*(3), L03605.

van Haren, H., Gostiaux, L., Morozov, E., & Tarakanov, R. (2014). Extremely long Kelvin-Helmholtz billow trains in the Romanche fracture zone. *Geophysical Research Letters*, *41*, 8445–8451.

Winters, K. B., & D'Asaro, E. A. (1996). Diascalar flux and the rate of fluid mixing. *Journal of Fluid Mechanics.*, *317*, 179–193.

Wright, L., Yang, Z., Bornhold, B., Keller, G., Prior, D., Wiseman, W., et al. (1986). Short period internal waves over the Huanghe (Yellow River) delta front. *Geo-Marine Letters*, *6*(2), 115–120.